

# Ash plume properties retrieved from infrared images: a forward and inverse modeling approach

Matteo Cerminara<sup>a,b,1,\*</sup>, Tomaso Esposti Ongaro<sup>b</sup>, Sébastien Valade<sup>c</sup>,  
Andrew J.L. Harris<sup>d</sup>

<sup>a</sup>*Scuola Normale Superiore di Pisa, Italy*

<sup>b</sup>*Istituto Nazionale di Geofisica e Vulcanologia, Sezione di Pisa, Italy*

<sup>c</sup>*University of Florence, Department of Earth Sciences, Italy*

<sup>d</sup>*Université Blaise Pascal, Laboratoire Magmas et Volcans, Clermont-Ferrand, France*

---

## Abstract

We present a coupled fluid-dynamic and electromagnetic model for volcanic ash plumes. In a forward approach, the model is able to simulate the plume dynamics from prescribed input flow conditions and generate the corresponding synthetic thermal infrared (TIR) image, allowing a comparison with field-based observations. An inversion procedure is then developed to retrieve ash plume properties from TIR images.

The adopted fluid-dynamic model is based on a one-dimensional, stationary description of a self-similar (top-hat) turbulent plume, for which an asymptotic analytical solution is obtained. The electromagnetic emission/absorption model is based on the Schwarzschild's equation and on Mie's theory for disperse particles, assuming that particles are coarser than the radiation wavelength and neglecting scattering. In the inversion procedure, model parameters space is sampled to find the optimal set of input conditions which minimizes the difference between the experimental and the synthetic image. Two complementary methods are discussed: the first is based on a fully two-dimensional fit of the TIR image, while the second only inverts axial data. Due to the top-hat assumption (which overestimates density and temperature at the plume margins), the one-dimensional fit results to be more

---

\*Corresponding author. Tel.: +393381272966.

*Email address:* [matteo.cerminara@gmail.com](mailto:matteo.cerminara@gmail.com) (Matteo Cerminara)

<sup>1</sup>Present address: Istituto Nazionale di Geofisica e Vulcanologia, Sezione di Pisa, via della Faggiola 32, 56126, Pisa, Italy.

accurate. However, it cannot be used to estimate the average plume opening angle. Therefore, the entrainment coefficient can only be derived from the two-dimensional fit.

Application of the inversion procedure to an ash plume at Santiaguito volcano (Guatemala) has allowed us to retrieve the main plume input parameters, namely the initial radius  $b_0$ , velocity  $U_0$ , temperature  $T_0$ , gas mass ratio  $n_0$ , entrainment coefficient  $k$  and their related uncertainty. Moreover, coupling with the electromagnetic model, we have been able to obtain a reliable estimate of the equivalent Sauter diameter  $d_s$  of the total particle size distribution.

The presented method is general and, in principle, can be applied to the spatial distribution of particle concentration and temperature obtained by any fluid-dynamic model, either integral or multidimensional, stationary or time-dependent, single or multiphase. The method discussed here is fast and robust, thus indicating potential for applications to real-time estimation of ash mass flux and particle size distribution, which is crucial for model-based forecasts of the volcanic ash dispersal process.

*Keywords:* Volcanic ash plume, Infrared imaging, Thermal camera, Inversion, One-dimensional model, Dynamics, Mass flow, Particle size

---

## 1. Introduction

Volcanic plumes are produced during explosive eruptions by the injection of a high-temperature gas-particle mixture in the atmosphere. The dynamics of ascent of a volcanic plume injected into the atmosphere is controlled by several factors (including vent overpressure, crater shape, wind) but, following Morton et al. (1956) and Wilson (1976) it has been recognized that mass flow rate (or eruption intensity) and mixture temperature mainly control the final plume height in stratified environments. In convective regimes and for the most intense eruptions, volcanic plumes are able to reach stratospheric layers, where ash can persist for years and affect climate, mesoscale circulation, air quality and endanger aviation transports. Due to their associated fallout, even weak volcanic plumes can have large impacts on populations living close to the volcano, especially in highly urbanized regions around active volcanoes.

Despite the advancement of physical models describing eruption conditions and the subsequent atmospheric dispersal of the gas-particle mixture

during an explosive eruption, one of the main obstacles to the full understanding of volcanic plume dynamics is the difficulty in obtaining measurements of the ascent dynamics and plume properties. Indeed, not only are measurements difficult and dangerous, but repeatability is an issue: eruptions differ from each other (even at the same volcano) and are too infrequent to allow construction of a statistically robust data set (Deligne et al., 2010). While this is certainly true for large eruptions (exceeding  $0.1 \text{ km}^3$  of total erupted mass, or a Volcanic Explosive Index – VEI  $> 3$  – Newhall and Self, 1982), persistent but low intensity explosive activity is common at several volcanoes such as Stromboli (Giberti et al., 1992; Harris and Ripepe, 2007), Santiaguito (Bluth and Rose, 2004; Johnson et al., 2004; Sahetapy-Engel and Harris, 2009b) and Soufriere Hills (Druitt and Kokelaar, 2002; Clarke et al., 2002). Such systems offer natural laboratories where methodologies and models for application to rarer, but more energetic events, can be prepared and tested. However, even in such cases, direct measurement in syneruptive conditions is extremely difficult, so that volcanologists must rely on indirect (remote sensing) measurement techniques.

Our current understanding of volcanic plume dynamics is largely based on visual observations and on one-dimensional plume models. However, there is a general consensus that the fundamental mechanism driving the ascent of volcanic plumes is the conversion of its thermal energy into kinetic energy through the quasi-adiabatic expansion of hot volcanic gases and atmospheric air entrained by turbulence (Sparks et al., 1997). One-dimensional models translating this concept into mathematical language (Wilson, 1976; Woods, 1988) have played a key role in advancing our understanding of the physics of volcanic plumes. One of the reasons of their success is also that simple models rely on simple measurements for validation, allowing solution with a limited number of parameters. In the case of eruption plume models, one observable is sufficient, namely plume height. This can be measured using photogrammetry, infrared imaging, satellite remote sensing, ceilometers, radio and radio-acoustic sounding (Tupper et al., 2003). Only one adjustable parameter is then needed to fit plume observations, namely a self-similarity coefficient, or the entrainment coefficient. This linearly correlates the rate of entrainment to the average vertical plume velocity (Ishimine, 2006).

However, the plume interior is generally invisible to the observer, and there is no way to measure mixture density from simple visual observation. As a result other electromagnetic imaging techniques (here defined as the process by which it is possible to observe the internal part of an object which

cannot be seen from the exterior) are needed to obtain data regarding the plume interior (Scollo et al., 2012).

Forward looking infrared (FLIR) cameras have become affordable in the last years and their use in volcanic plume monitoring has become popular (Spampinato et al., 2011; Ramsey and Harris, 2012; Harris, 2013). To date they have been used to classify and measure bulk plume properties, such as plume front ascent rates, spreading rates and air entrainment rates for both gas, ash and ballistic rich emissions (Harris and Ripepe, 2007; Patrick et al., 2007; Sahetapy-Engel and Harris, 2009b), analysis of particle launch velocities, size distributions and gas densities (Harris et al., 2012; Delle Donne and Ripepe, 2012) and particle tracking velocimetry (Bombrun et al., 2013). Recent deployments have involved use of two thermal cameras: one close up to capture the at-vent dynamics as the mixture exits from the conduit and one standing off to obtain full ascent dynamics as the plume ascends to its full extent. This has been coupled with stereo-visible-camera, Doppler radar measurements of the same plume and infrasonic measurement, to detect large-scale puffing and eddies. Recently, Valade et al. (2014) have developed a procedure to extract from thermal infrared (TIR) images an estimate of the entrainment coefficient and other plume properties including plume bulk density, mass, mass flux and ascent velocity.

However, recovery of the plume ash mass content and grain size distribution in near-real time remains a major challenge. Such data are crucial for hazard mitigation issues, and especially for the Volcanic Ash Advisory Centers (VAACs) which issue advisories to the aviation community during explosive eruptions. Indeed, VAACs use ash dispersion models (VATD, Volcanic Ash Transport and Dispersion models) to forecast the downstream location, concentration, and fallout of volcanic particles (Stohl et al., 2010). However, to be accurate, such models require quantification of the plume ash concentration and particle size distribution (Mastin et al., 2009; Bonadonna et al., 2012).

In this work we show that recovering this information is possible in a rapid and robust fashion by comparing thermal infrared images that record the emission of a volcanic plume, with synthetic thermal infrared images reconstructed from analytical models.

Our approach inverts time-averaged thermal image data to reconstruct the temperature, ash concentration, velocity profiles and the grain size distribution within the plume. To do this we construct a synthetic thermal image of the volcanic plume starting from the spatial distribution of gas and

particles obtained from a fluid dynamic model. The method is based on the definition of the infrared (IR) irradiance for the gas-pyroclast mixture. This is derived from the classical theory of radiative heat transfer (Modest, 2003) with the approximation of negligible scattering (Schwarzschild’s equation). The model needs to be calibrated to account for the background atmospheric IR radiation and the material emissivity (Harris, 2013). The absorption and transmission functions needed to compute the irradiance are derived from the Mie’s theory (Mie, 1908) and can be related, by means of semi-empirical models, to the local particle concentration, grain size distribution and to the optical thickness of the plume. By applying such an IR emission model to the gas-particle distribution obtained from a fluid dynamic model it is possible to compute a synthetic thermal image as a function of the input conditions. We adopt a one-dimensional, time-averaged plume model derived from the Woods (1988) model to simulate the plume profile. The advantage of 1D modeling is that inversion can be performed in a fast and straightforward way by means of minimization of the difference between a synthetic and a measured IR image. However, the method is applicable to any kind of plume model.

Thus, In Section 2 we present the IR electromagnetic model (equations and approximations) that we use to produce plume synthetic images. In Section 3 we describe the one-dimensional integral fluid-dynamic model of the plume. In Section 4 we apply the coupled fluid-dynamic-electromagnetic model (forward model) to construct a synthetic thermal image of a volcanic plume. In Section 5 we use this model to invert experimental TIR data acquired during an explosive event at Santiaguito volcano (Guatemala) to estimate the flow conditions at the vent. Figure 1 illustrates the methodology and models developed in the paper.

## 2. Electromagnetic model

Due to the high-temperature of erupted gas and pyroclasts, volcanic plumes emit electromagnetic radiation in the thermal infrared (TIR) wavelengths (8–14  $\mu\text{m}$ ). Every single particle radiates as a function of its temperature (through the Planck’s function) and material properties (each material being characterized by its *emissivity* – see Sect.2.3). On the other hand, part of the emitted radiation is absorbed by neighbouring gas and particles, so that the net transmitted radiation results from the balance between emission

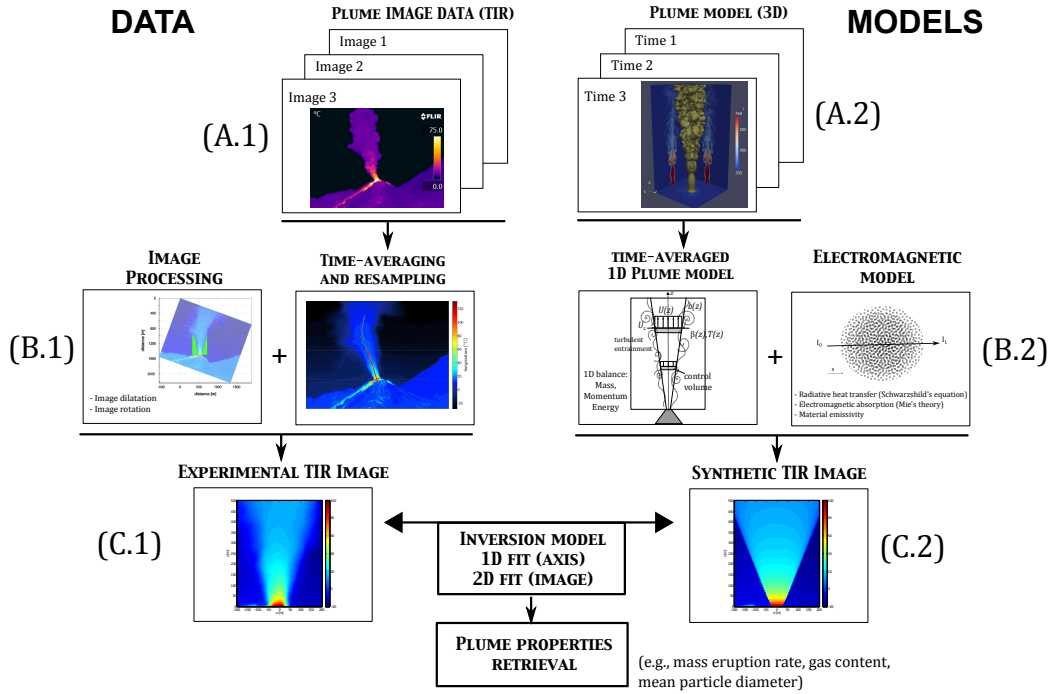


Figure 1: Schematic overview of the aims and methodology of the work presented in this paper. (A.1) Volcanic plume emission is recorded using a thermal infrared (TIR) camera. Modeling of such phenomenon requires 3D numerical models (A.2), able to reproduce the complex fluid-dynamic behavior at various length and time scales. However because such models require high computational power and time, analytical 1D mean plume models (B.2) may be used to predict the mean behaviour of volcanic plumes. Such models are time-averaged stationary models, which describe the mean spatial distribution of flow parameters (e.g., particle concentration, temperature, velocity) given a set of input conditions. By coupling an electromagnetic model to the plume model, we simulate the TIR emission of the gas-particle mixture, and compute a synthetic thermal infrared image (C.2). The mean plume behaviour may also be recovered from the recorded image by constructing a "mean image" (B.1), which is a time-averaged image obtained from averaging a sequence of images in a TIR video sequence. In doing this, the time-dependent dynamic fluctuations of the plume are filtered, leaving an image that reflects the mean plume behaviour. Image processing is then applied to obtain an image with a vent-centered metric coordinate system, comparable to that created by the forward model. Recursive minimization of the discrepancy between the observed and modeled TIR images is then performed by application of an inversion model (2D when the entire images are compared, or 1D when only the plume central axis is compared), which searches for the best model input-parameters (e.g., ash mass, particle size distribution, etc.) that reproduce the observed data.

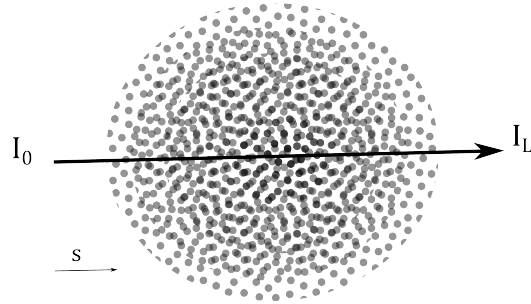


Figure 2: Schematic configuration of the propagation of a TIR ray inside a heterogeneous medium. The absorption coefficient is proportional to particle concentration. TIR intensity changes along the path due to particle emission/absorption. We indicate with  $s$  the curvilinear coordinate along the path, with  $I_0$  being the background intensity and  $I_L$  being the measured intensity at distance  $L$  from the background position.

and absorption and is a function of the electromagnetic wavelength  $\lambda$ . This balance is expressed by Schwarzschild's equation.

### 2.1. Schwarzschild's equation

Along an optical path, defined by a curvilinear coordinate  $s$  (see Fig. 2), the infinitesimal variation of TIR intensity due to emission at temperature  $T$  is proportional to the Planck function  $B = B_\lambda(T)$  multiplied by the infinitesimal length  $ds$ :  $dI_{emit} = \beta_e B ds$ . On the other hand, the infinitesimal variation due to absorption is proportional to the radiation intensity itself, so that  $dI_{abs} = \beta_a I ds$ . Following Kirchoff's law, the emission and absorption coefficients are equal  $\beta_e = \beta_a = K$ , so that, along a ray, this balance is expressed by:

$$\frac{dI}{ds} = K(B - I). \quad (1)$$

By solving Eq.(1) along the optical path (as represented in Figure 2), for a heterogeneous medium, we find that

$$I_\lambda(L) = I_0 e^{-\tau_L} + \int_0^L K_\lambda(s) B_\lambda(s) e^{-(\tau_L - \tau(s))} ds \quad (2)$$

where  $I_0 = I(0)$  is the background atmospheric radiation at the given wavelength and the integral is computed along a straight ray from the source

$s = 0$  to  $s = L$ , this being the detector position. The *optical thickness* is defined as:

$$\tau(s) = \int_0^s K(s)ds \quad (3)$$

and  $\tau_L = \tau(L)$ . Because the medium is heterogeneous (i.e., it can have a non-homogeneous particle concentration and temperature) the absorption coefficient  $K$  depends on the position  $s$  along the optical path. In the next section, we show how  $K(s)$  can be derived for a cloud of particles.

## 2.2. Absorption coefficient of the particulate phase

The absorption coefficient for a cloud of disperse spherical particles can be derived from Mie's theory (Mie, 1908; Hänel and Dlugi, 1977). Up to a limiting size  $r_\lambda$ , which depends on the measurement wavelength (see Fig. 1 of Hänel and Dlugi, 1977),  $K$  can be described by a power law. Above the upper particle size limit, absorption no longer depends on the particle size or material, but simply corresponds to the total cross section of the dispersed particles:

$$K = \frac{1}{V} \sum_{j=1}^N \pi r_j^2$$

where  $r_j$  is the radius of the single sphere and  $V$  is the total volume occupied by the mixture. For the case of volcanic particles, this condition is almost always satisfied when particles are much larger than the measurement wavelength (about 10  $\mu\text{m}$ ).

By expressing the volume  $V$  in terms of the density and particle concentration  $\varepsilon$ , the absorption coefficient can be set proportional to the Sauter diameter  $d_s$  of the particle distribution, i.e.

$$K = \frac{3}{4} \varepsilon \frac{\sum_j r_j^2}{\sum_j r_j^3} = \frac{3}{2} \frac{\varepsilon}{d^3/d^2} = \frac{3}{2} \frac{\varepsilon}{d_s} \quad (4)$$

or, in terms of the particle microscopic density  $\hat{\rho}_s$  and the particle bulk density ( $\rho_s = \varepsilon \hat{\rho}_s$ )

$$K_s = \frac{3}{2d_s \hat{\rho}_s} \rho_s = A_s \rho_s \quad (5)$$

Here we have introduced the specific absorption coefficient of the particles  $A_s$  which represents the cross section of the particulate phase per unit of mass



(having the dimensions of  $[\text{m}^2/\text{Kg}]$ ). The Sauter diameter  $d_s$  represents the mean particle diameter that gives the same volume/surface area ratio as the original particle size distribution. For example, we can estimate the mean Sauter diameter in the case of a log-normal grain size distribution. This is a common hypothesis in volcanology when we assume that the grain size distribution is Gaussian in  $\phi = -\log_2(d)$  units, with mean  $\mu$  and standard deviation  $\sigma_{\text{gsd}}$ . In such case, we can write the normalized particle distribution (in millimeters) as:

$$f(x; \mu, \sigma_{\text{gsd}}) = \frac{1}{x \ln(2) \sigma_{\text{gsd}} \sqrt{2\pi}} e^{-\frac{(\log_2(x) + \mu)^2}{2\sigma_{\text{gsd}}^2}}$$

and the Sauter mean diameter can be computed analytically as

$$d_s = 2^{-\mu + \frac{5}{2} \log(2) \sigma_{\text{gsd}}^2}. \quad (6)$$

This means that the mean particle diameter “seen” by the TIR sensor is always larger than the mean diameter  $\bar{d} = 2^{-\mu + \frac{1}{2} \log(2) \sigma_{\text{gsd}}^2}$ .

In the context of non-homogeneous mixtures, the particle volumetric fraction  $\varepsilon$  in Eq.(4) changes with the position  $s$  along the ray trajectory, i.e.,  $K = K(s) = \frac{3}{2} \frac{\varepsilon(s)}{d_s}$ . If the grain size distribution changes locally, the dependency of  $d_s(s)$  should also be taken into account.

In Section 4 we will detail how the optical thickness  $\tau(s)$  and Eq.(2) are computed in volcanic plume applications.

### 2.3. Emissivity of the particulate phase

To estimate the emitted electromagnetic intensity, we assume that pyroclastic particles behave as *gray bodies*. The ratio between the emitted radiation and the black-body intensity at the same temperature (given by the Planck function) is described by the *emissivity* coefficient, indicated by  $\epsilon$ . For pyroclastic particles at FLIR wavelengths (8–14  $\mu\text{m}$ ), if the mixture is a trachyte/rhyolite, then an emissivity of 0.975 is appropriate (Harris, 2013). Thus to convert between spectral radiance and kinetic temperature we use:

$$B_\lambda(T) = \epsilon \frac{2hc^2}{\lambda^5} \frac{1}{e^{\frac{hc}{\lambda k_B T}} - 1} \quad (7)$$

where  $h$  is the Planck’s constant,  $c$  is the speed of light,  $k_B$  is the Boltzmann’s constant and  $T$  is the temperature.

#### 2.4. Absorption by atmospheric and volcanic gases

Thermal cameras installed to video volcanic plumes are typically installed at distances of several kilometers from the source. This allows safe measurements, and the full ascent history from vent to point of stagnation to be imaged. Over such distances, the effect of atmospheric absorption will be non-negligible (Harris, 2013). This effect becomes more important as humidity increases, because water droplets have high absorption properties at TIR wavelengths. Volcanic gases also have a significant effect on absorbing emitted radiation in the TIR (Sawyer and Burton, 2006). Therefore, to apply Eq.(2) the absorption coefficients of the atmospheric and volcanic gases need be taken into account.

Absorption by gases can be computed using Eq.(1), so that the resulting coefficient is the sum of the coefficient of the  $N_{ph}$  phases, whereas the emissivity is a weighted average:

$$K_{mix} = \sum_j^{N_{ph}} K_j; \quad \epsilon_{mix} = \frac{\sum_j^{N_{ph}} K_j \epsilon_j}{K_{mix}}$$

Analogously to the expression of  $K_s$  for particles, the absorption coefficient for gases can also be expressed as the product of the specific absorption coefficient  $A_j$  (which depends only on gas material properties) times the gas bulk density  $K_j(\mathbf{x}) = A_j \rho_j(\mathbf{x})$ .

For example, in volcanic ash plumes we may want to consider the presence of water vapor, carbon and sulphur dioxide. In such a case, at any point  $\mathbf{x}$ :

$$K_{mix} = \sum_j^{N_{ph}} K_j = \sum_j^{N_{ph}} A_j \rho_j(\mathbf{x}); \quad j = s, H_2O, CO_2, SO_2, Air \quad (8)$$

For typical eruptive conditions (involving water vapour as the main volcanic gas),  $A_s$  and  $A_w$  are of the same order of magnitude. Fig. C.13 shows the absorption coefficient for atmospheric water vapor at sea level. The specific absorption coefficient is obtained by dividing by the corresponding density, obtaining  $A_w \simeq 1$  in the waveband 8–14  $\mu\text{m}$ . It is important to notice that, whereas specific absorption coefficients for particles are almost independent from the wavelength (under the assumptions of large particles)

for gases this dependency can be significant. We therefore consider that the coefficients  $A_j$  for gases represent an average value over a relatively narrow band, corresponding to the wavelength window of TIR detectors (8–14  $\mu\text{m}$ ).

### 2.5. Atmospheric background radiation

The background atmospheric radiation (the first term of Eq.2) also contributes to the detected TIR radiance. Whereas the center of an ash plume is generally opaque to transmission of background thermal radiation (meaning that this term is negligible along an optical path crossing the axis of an ash plume), part of the background atmospheric radiation can be transmitted through a gaseous plume or through the diffuse margins of an ash-laden plume, where particle concentration is much lower. The treatment of background radiation begins with an estimate of the spectral radiance in the absence of the plume at a distance  $L$  from the source,  $L$  being larger than the distance of the observer from the plume axis (see Fig. 4). We will show in Section 5 how this can be done in practical cases.

In summary, the at-detector spectral radiance  $I_\lambda(L)$  at wavelength  $\lambda$  associated to emission/absorption balance from a gas-particle mixture in the atmosphere can be computed using an electromagnetic model by specifying the following variables and parameters along each optical path received by a detector:

- the Sauter diameter  $d_s$  of the particle distribution (Eq. 4);
- the spatial distribution of particle volumetric concentration  $\varepsilon$  (Eq. 4);
- the spatial distribution of temperature  $T$  (Eq. 7);
- the material (either gas or solid) emissivity  $\epsilon$  (Eq. 7);
- the specific absorption coefficients  $A_j$  for each gas species (Eq. 8);
- the bulk density distribution  $\rho_j$  of each gas species (Eq. 8).

Whereas material properties (emissivity, specific absorption coefficients) can be obtained from laboratory measurements, the spatial distribution of gas and particles, plus their variation in density and temperature need to be derived from a fluid-dynamic model that describes the dynamics of the volcanic plume for specific vent conditions.

### 3. Plume model

In this section, we present a one-dimensional fluid-dynamic model that can be applied to reconstruct the particle concentration and temperature distribution in the volcanic plume to allow computation of the IR radiation field. In Section 5 we will adopt this model to solve the inverse problem.

Our model is based upon the Woods (1988) model, which describes the transport of volcanic ash and gases in the atmosphere assuming a *dusty gas* approximation (Carrier, 1958; Marble, 1970). Accordingly, full local kinetic and thermal equilibrium between gas and particles are assumed, i.e. all components of the eruptive mixture are assumed to have the same velocity and temperature fields. In this work we will assume that the erupting mixture is composed of volcanic gas (subscript  $e$ ), solid particles (subscript  $s$ ) and atmospheric gas (subscript  $\alpha$ ). We denote the dusty-gas mixture with subscript  $\beta$ . Thermodynamic properties of the dusty gas are reported in Appendix A.

Woods' transport model can be derived formally from the full three-dimensional dusty-gas model under the following assumptions (Morton et al., 1956; Morton, 1959; Wilson, 1976; List, 1982; Papanicolaou and List, 1988; Woods, 1988; Fanneløp and Webber, 2003; Kaminski et al., 2005; Ishimine, 2006; Plourde et al., 2008):

- The Reynolds number is large and turbulence is fully developed, so that thermal conduction and viscous dissipation can be neglected.
- Pressure is constant across a horizontal section and is adjusted to atmospheric pressure at the vent (i.e., the model cannot be applied to underexpanded jets).
- The plume is *self-similar*, i.e., the time-averaged profiles of vertical velocity, density and temperature across horizontal sections at all heights have the same functional form (either *top-hat* or Gaussian).
- The time-averaged velocity field outside and near the plume edge is horizontal.
- Stationary input conditions and steady atmosphere (no wind).
- Radial symmetry around the source.

We seek an axisymmetric solution in a poloidal plane  $(r, z)$  (with unit vectors  $(\hat{r}, \hat{z})$ ) of the dusty gas conservation equations with the following form:

$$\rho(r, z) = \begin{cases} \beta(z), & \text{if } 0 \leq r < b(z) \\ \alpha(z), & \text{if } r \geq b(z) \end{cases} \quad (9)$$

$$u(r, z) = \begin{cases} +U(z)\hat{z}, & \text{if } 0 \leq r < b(z) \\ -U_\epsilon(z)\hat{r}, & \text{if } r = b(z) \\ -u_\epsilon(r, z)\hat{r}, & \text{if } r > b(z) \\ u_\epsilon \rightarrow 0 & \text{if } r \gg b(z) \end{cases} \quad (10)$$

$$p(r, z) = p(z) \quad (11)$$

$$T(r, z) = \begin{cases} T_\beta(z), & \text{if } 0 \leq r < b(z) \\ T_\alpha(z), & \text{if } r \geq b(z) \end{cases} \quad (12)$$

where  $\rho$ ,  $u$ ,  $p$  are the flow density, velocity and pressure,  $b$  is the plume radius,  $U$  is the plume axial velocity and  $U_\epsilon$  is the entrainment velocity. Here we assume a “top hat” self-similar profile (i.e., a constant profile) for all variables, so as to simplify computation with a view to efficiently solve the inverse problem. By imposing the top-hat plume solution, the resulting mass, momentum and energy balance equations read (Woods, 1988):

$$\begin{cases} d_z(\rho_j U b^2) = 0 & (j = s, e) \\ d_z(\beta U b^2) = 2\alpha b U_\epsilon \\ d_z(\beta U^2 b^2) = (\alpha - \beta) g b^2 \\ d_z(\beta U b^2 C_\beta T_\beta) = (C_\alpha T_\alpha) d_z(\beta U b^2) + \frac{U^2}{2} d_z(\beta U b^2) - g \alpha U b^2. \end{cases} \quad (13)$$

The first equations state that the mass fluxes of volcanic gases and particles must be conserved, so that their value is constant along the plume axis ( $\rho_j(z)$  is their bulk density).  $g$  is the gravity acceleration. The remaining unknowns are  $\beta(z)$ ,  $U(z)$ ,  $b(z)$  and  $T_\beta(z)$ . The system is closed by opportune equations of state expressing the mixture density as a function of temperature  $\beta = \beta(T_\beta)$  (thermal equation of state) and specific heats  $C_\beta$  and  $C_\alpha$  (caloric equation of state). For a dusty gas, thermodynamic properties are computed locally from the properties of each component of the mixture. Thermodynamic closure equations are reported in Appendix A.

Finally, the ambient density  $\alpha(z)$ , the ambient temperature  $T_\alpha(z)$  and the dependence of  $U_\epsilon$  on other unknowns (the entrainment model) must be

given. For the atmosphere, we assume a linear temperature decrease at a constant rate in the troposphere (as is appropriate for weak plumes) and a hydrostatic density profile. The entrainment velocity  $U_e$  is expressed as  $U_e = kU\eta(\beta/\alpha)$ , where  $k$  is a dimensionless entrainment coefficient and  $\eta$  is an arbitrary function of the density ratio (Fanneløp and Webber, 2003). When  $\eta = 1$  we recover the model of Morton et al. (1956), and if  $\eta(x) = \sqrt{x}$  we obtain the model of Ricou and Spalding (1961). In this work, we will always assume  $\eta = 1$ .

Following Fanneløp and Webber (2003), we also define some new compound variables :

$$Q_j = \rho_j Ub^2 \quad (j = s, e) \quad (14)$$

$$Q = \beta Ub^2 \quad (15)$$

$$M = \beta U^2 b^2 \quad (16)$$

$$F = \left[ (\alpha - \beta) + \alpha \frac{\chi Q_m}{Q - Q_m} \right] Ub^2 \quad (17)$$

This allows the transport equations to be expressed in a more compact form.

In Eq. (17),  $Q_m = Q_s - (\psi_e - 1)Q_e$  and  $\chi = \frac{(\chi_s - 1)Q_s + (\chi_e - 1)Q_e}{Q_m}$ . Note that  $Q_m = Q_s$  if the emitted gas is identical to the atmospheric gas ( $\psi_e = R_e/R_\alpha = 1$ ) whereas  $\chi$  accounts for the difference in the caloric properties of the erupted mixture with respect to the atmosphere.

The expression for  $F$  (Eq. 17) represents a modification of the buoyancy flux for a dusty-gas plume. It takes the classical form  $F = (\alpha - \beta)Ub^2$  (Fanneløp and Webber, 2003) for  $Q_m = 0$ , i.e. for a single-component gas plume. It is also convenient to introduce the non-dimensional variables  $\zeta = z/L$ ,  $q = Q/Q_0$ ,  $m = M/M_0$  and  $f = F/F_0$ , where  $L = \frac{Q_0}{\sqrt{\alpha_0 M_0}}$  and the subscript 0 indicates values at  $\zeta = 0$ . We also define  $q_m = Q_m/Q_0$  and  $\phi = F_0/Q_0$ .

The general form of equation (13) in terms of the new variables ( $q, m, f$ ) can be solved numerically as a function of the vent conditions, namely the vent radius, the mass flow rate of all gaseous and solid components and its temperature (Cerminara, 2014). By transforming back into the dimensioned variables (algebraic transformations are reported in Appendix B), numerical results provide, at each height, the mixture bulk density  $\beta(z)$ , vertical velocity  $U(z)$ , temperature  $T_\beta(z)$  and plume radius  $b(z)$ . The bulk density of all dusty-gas components  $\rho_j(z)$  can then be computed, and the

three-dimensional distribution of all variables can be recovered from the one-dimensional results by applying the self-similarity hypothesis (Eqs.9–12).

### 3.1. Approximate solution of the plume model

Instead of solving the complete model of Eq. (13), in this work we adopt a simplified plume model. This further decreases computation time. This approximation asymptotically describes the dusty-plume dynamics within the Boussinesq limit (i.e., for small density contrasts) and for a non-stratified atmosphere. This regime is similar to that explored by Morton et al. (1956) for single-phase gas plumes. Such an approximation holds for an intermediate region “far enough” from the vent and “well below” the maximum plume height (where neutral buoyancy conditions are reached). These conditions are met for  $q \gg q_m$  and  $q \gg f$ . Because, in this regime, the modified buoyancy flux is constant  $f = 1$ , the second condition reduces to  $q \gg 1$ , which is satisfied far enough from the vent (after sufficient air has been entrained). To be more quantitative,  $4b(0) < z < H$  where  $H = \frac{\gamma RT}{g} \approx 10$  km is the typical length scale for atmospheric stratification.

In this approximation, the system of equations (13) reduces to (Cerninara, 2014):

$$\begin{cases} d_\zeta(q) = v_q \sqrt{m} \\ d_\zeta(m) = v_m \frac{q}{m} \\ d_\zeta(f) = 0 \end{cases} \quad (18)$$

where we have introduced the following parameters:

$$v_q = 2k \quad (19)$$

$$v_m = \frac{gF_0Q_0^2}{\alpha_0^{1/2}M_0^{5/2}}(1 - \gamma) \quad (20)$$

$$\gamma = \frac{(\chi + 1)q_m}{\phi} \quad (21)$$

This system is formally equivalent to the Morton et al. (1956) equations but with different dimensional constants  $v_q$  and  $v_m$ . These now account for the multiphase nature of the erupting mixture. Morton’s equations are recovered by setting  $\gamma = 0$  and  $\chi = 0$  (single phase plume).

Eqs. (18) have an asymptotic analytical solution expressed by:

$$\begin{cases} q(\zeta) = \sqrt{\frac{4v_q}{5v_m} \left[ \left( \frac{3}{4} \sqrt{\frac{4v_q v_m}{5}} \zeta + 1 \right)^{10/3} + \frac{5v_m}{4v_q} - 1 \right]} \\ m(\zeta) = \left[ \frac{3}{4} \sqrt{\frac{4v_q v_m}{5}} \zeta + 1 \right]^{4/3} \\ f(\zeta) = 1 \end{cases} \quad (22)$$

which also has the correct asymptotic behaviour for  $\zeta \gg 1$ . This solution can be viewed as a function of the boundary values of the flow variables and the model parameters, namely  $(v_q, v_m, L, \phi, \chi, q_m)$ .

In Figure 3 we compare the numerical solution of Eq. 13 with the analytical solution of Eq. 22, assuming vent conditions for a typical weak plume at Santiaguito (Sahetapy-Engel and Harris, 2009b; Valade et al., 2014), as reported in Tab. 1 and discussed in Sect. 5. Consistently with this approximation, the analytical solution closely fit the complete model solution in the central part of the plume. However, it differs near  $z = 0$  and near the plume top. Note that the density and temperature profiles (plots c) and d) have been derived from the non-dimensional variables  $(q, m, f)$  by using the stratified atmospheric profiles  $\alpha(z)$  and  $T_\alpha(z)$  into Eqs. (B.1) and (B.4). In this way we have taken into account atmospheric stratification while maintaining the simple structure of the equations of Morton's approach (which holds in a non-stratified environment).

#### 4. Coupled forward model

We assume that the bulk density  $\rho_j$  of each gaseous and solid component is given at every point of the domain (Figure 4). For each component, the specific absorption coefficients  $A_j$  and emissivity  $\epsilon_j$  (which depend only on the material) are assumed to be known. Now,

1. The absorption coefficient of the mixture  $K_{\text{mix}}$  can be estimated at any point by using Eq. 8.
2. Along every ray in Figure 4 we can compute the optical thickness  $\tau(s)$  (Eq. 3) by integrating  $K_{\text{mix}}$  along the ray trajectory (which is assumed to be a straight line).
3. We can compute the Planck function of the mixture (Eq. 7) at each point of the domain as a function of the local temperature and the local mixture emissivity.



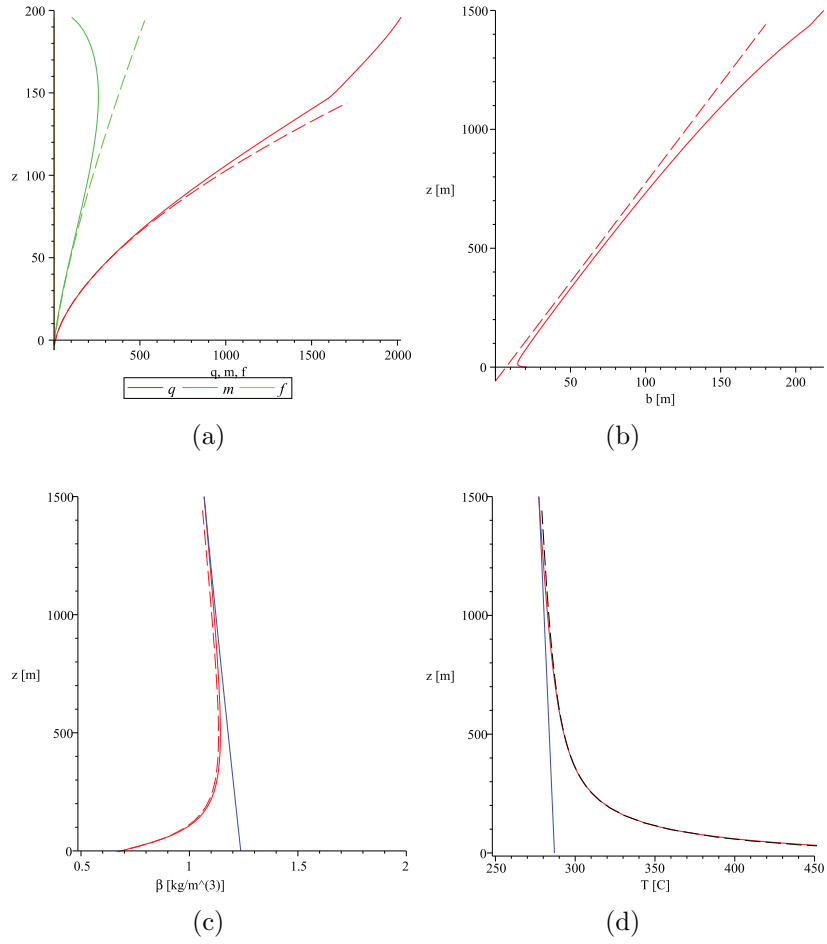


Figure 3: Comparison between the numerical solution of the Woods (1988) model (solid lines) and the approximated analytical solution (Eq. 22, dashed lines). a) Non-dimensional variables ( $q, m, f$ ) as a function of the non-dimensional length scale  $\zeta$ ; b) dimensioned plume radius  $b(z)$ ; c) plume density  $\beta(z)$  (Eq. B.1); d) plume temperature  $T_\beta(z)$  (Eq. B.4). The straight solid lines represent the atmospheric profiles.

$U_0$	5 m/s
$T_0$	578 °C
$b_0$	21 m
$Q_e$	571 kg/s
$Q_s$	414 kg/s
$\frac{dT_\alpha}{dz}$	- 4.4 °C/km
$T_{\alpha 0}$	15 °C
$k$	0.1
$\beta_0$	0.447 kg/m <sup>3</sup>
$n$	0.58
$Q$	985 kg/s

Table 1: Initial and boundary conditions of weak plume simulation.

4. Finally, the background radiation  $I_0$  is estimated at some point behind the plume (e.g., at  $s = 0$  in Fig. 4), taken as the image horizon.

With these ingredients, we can compute the radiation intensity along a discrete number of rays forming the electromagnetic image of the domain  $\Omega$ . It is worth noting that, usually, commercial devices give the temperature as output image, not the intensity. To derive the temperature image from the TIR intensity, the Planck function has to be inverted.

#### 4.0.1. Geometric approximations

To simplify the problem, we have adopted the following geometric approximations:

- the camera is far enough from the plume so that rays can be considered as parallel;
- rays are assumed to cross the plume axis orthogonally;
- effect of plume bending (eventually due to wind) are corrected by means of image processing techniques.

With these hypotheses, the geometric configuration required to construct the IR image is sketched in Fig. 4b, where the plume axis is oriented normally to the image plane at  $r = 0$ . Radius  $b(z)$  depends on the height above the vent and the concentration and temperature fields are constant inside the circle and zero outside.

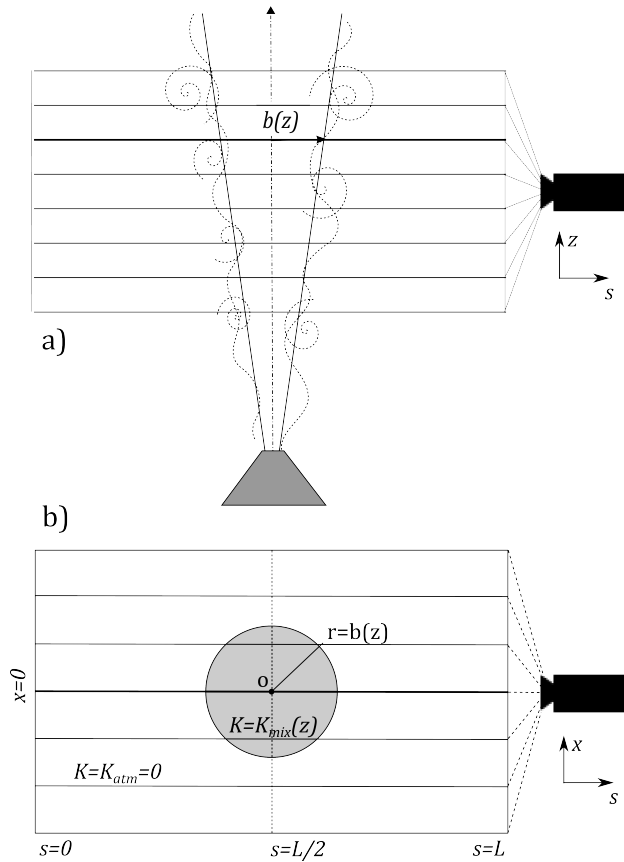


Figure 4: Geometric configuration adopted for the calculation of the IR intensity. a) Side view. b) Top view of a cutting plane orthogonal to the plume axis (point  $o$ ). The plume radius is represented by the gray-shaded region (top-hat approximation).

By adopting a top-hat assumption for the plume profile, the radiant intensity can be computed analytically under the further simplification that the emission/absorption of the atmosphere can be neglected (this is reasonable if the distance of the camera from the plume is not too large, indicatively less than about 10 km). In this case, the absorption coefficient is taken equal to zero outside the plume, whereas the value of  $K_{\text{mix}}(z)$  within the plume can be computed starting from the analytical solution of the plume model, by expressing the mixture density  $\beta$  in terms of the non-dimensional variable  $q$  (Eqs. B.1 and 22)

$$K_{\text{mix}}(z) = A_s \rho_s + A_e \rho_e = (A_s q_s + A_e q_e) \frac{\beta}{q} = (A_s q_s + A_e q_e) \alpha \frac{(q + \chi q_m)}{(\phi + q)(q - q_m)} \quad (23)$$

with  $K_{\text{mix}}(z)$  depending on  $z$  only through  $q = q(z)$ . We also define the specific absorption coefficient of the mixture

$$A_m = (A_s q_s + A_e q_e) \quad (24)$$

so that  $K_{\text{mix}} = A_m \beta / q$  and  $A_m$  is an initial mixture parameter that does not depends on the position along the plume.

With reference to Fig. 4b), along each ray we identify the points  $s_1$  and  $s_2$  where the ray crosses the edge of the plume. For  $-b < x < b$  their coordinates are  $s_1 = L/2 - \sqrt{b^2 - x^2}$  and  $s_2 = L/2 + \sqrt{b^2 - x^2}$  and the optical thickness is then simply

$$\tau(s, z) = \begin{cases} 0 & 0 < s < s_1 \\ K_{\text{mix}}(z) (s - s_1) & s_1 < s < s_2 \\ K_{\text{mix}}(z) (s_2 - s_1) & s_2 < s < L \end{cases} \quad (25)$$

Because in this example we have assumed that the optical thickness of the atmosphere is zero, we find that

$$\tau_L(z) = K_{\text{mix}}(z) (s_2 - s_1) = 2K_{\text{mix}}(z) \sqrt{b^2 - x^2} \theta(b^2 - x^2)$$

where  $\theta$  is the Heaviside step function. To compute the Planck constant, we also neglect possible variations in emissivity along the optical path and assume that  $\epsilon = 1$  across the plume. This is equivalent of assuming that the ash behaves as a black body (Harris, 2013). With these hypotheses, the Planck function depends only on the vertical coordinate  $z$  through  $T_\beta(z)$  (Eqs. B.4 and 7). By solving the integral, we obtain:

$$I_L(x, z) = I_0 e^{-\tau_L} + B(z) (1 - e^{-\tau_L}) \quad (26)$$

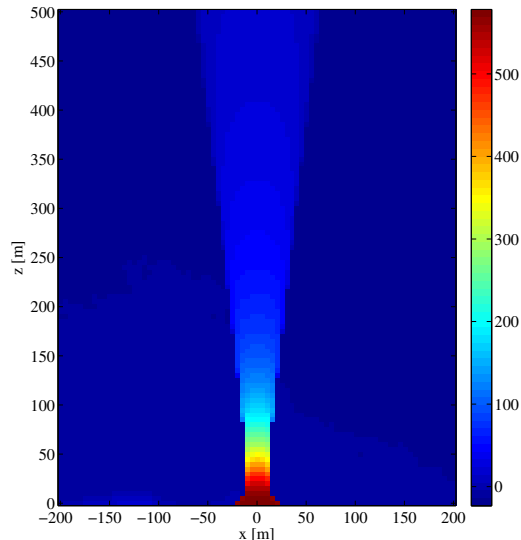


Figure 5: Synthetic IR image obtained from the 1D approximated model (Eq. (22)). The electromagnetic intensity  $I_L$  (Eq. 26) has been converted into a temperature image by means of the Planck’s equation (7).

In Figure 5 the synthetic TIR image of the plume given in Figure 3 is shown ( $I_0$  has been computed by assuming a uniform background temperature of 288K). The thermal image obtained from the approximated model does not appreciably differ from that obtained from the Woods’ model (not shown), because the profiles of radius, density and temperature are almost coincident (see Fig. 3b-d).

## 5. Inverse model and application

The coupled fluid–electromagnetic model described in the previous sections provides a synthetic infrared image of a gas–particle plume, that we have called  $I_L(x, z)$ . This is a complex, non-linear function of the flow conditions at the vent and of the material properties of volcanic gases and particles and of the atmosphere. More specifically, assuming that the material properties are known and neglecting the emission/absorption contribution of the atmosphere, the synthetic image can be expressed as a function of the plume model boundary values and parameters and of the specific absorption coeffi-

cient of the mixture  $A_m$  (given by Eq. 24):

$$I_L = I_L(v_q, v_m, L, \phi, \chi, q_m, A_m) \quad (27)$$

Using the algebraic transformations of Appendix C we can express  $I_L$  as a function of  $(b_0, U_0, T_0, n_0, k, d_s)$  where  $b_0, U_0, T_0, n_0$  are the plume radius, velocity, temperature and gas mass fraction at  $z = 0$ ,  $k$  is the air entrainment coefficient and  $d_s$  is the equivalent Sauter diameter of the grain size distribution. Note that  $z = 0$  may not correspond to the vent quota but instead to the minimum height of the acquired image. It is also worth recalling here that we assume that  $d_s$  does not change during plume development, i.e., that particle grain size distribution does not change in the plume. However, if this is not the case (e.g., because of the effect of particle loss from the plume margins – Woods and Bursik, 1991) the procedure can still be applied but the plume solution (Eq. 22) and the TIR radiation (Eq. 26) should be modified accordingly.

This synthetic image can now be compared to the actual TIR images captured during the volcanic event. We will demonstrate in this section how it is possible to estimate the parameters in Eq. 27 by means of inversion procedures. To do this, TIR images must be preliminary processed in order to obtain an average experimental intensity image  $I_E(x, z)$  and a background image  $I_0(x, z)$ . The minimum of the difference  $\|I_E - I_L\| = f(v_q, v_m, L, \phi, \chi, q_m, A_m)$  is then sought in the parameter space to find the eruptive conditions which best fit the observation.

### 5.1. Image processing

TIR video used here provide a sequence of  $N+1$  IR images  $P_i (i = 0, \dots, N)$  of a developing plume, acquired at a fixed time rate. Usually, commercial devices automatically convert the digital intensity image registered by the charge coupled device (CCD) into a 8 or 16 bit temperature image. We will here assume that the first image  $P_0$  represents the time immediately before the eruption and that  $P_1$  is the first image of the erupting plume. Because some time is needed for the plume to develop, we will also assume that the flow can be considered stationary between frames  $P_m$  and  $P_f$ . Under such assumptions, we can compute an average TIR image  $P_a = \frac{\sum_{i=m}^f P_i}{f-m+1}$ .

By means of image processing techniques (Valade et al., 2014) the plume trajectory is extracted from  $P_a$  and the region of interest along the axis is selected. If the plume axis is bent (as a result of wind or source anisotropy) the

images  $P_0$  and  $P_a$  are corrected by means of geometric transformations (rotation and dilatation). This is also used to correct possible image distortions associated to camera orientation.

Finally, Eq. (7) is applied to thermal images  $P_a$  and  $P_0$  to obtain the experimental intensity image  $I_E(x, z)$  and the atmospheric background  $I_0(x, z)$ , where  $z$  run along the axial direction and  $x$  along the horizontal direction perpendicular to the camera optical axis.

### 5.2. TIR dataset for an ashy plume at Santiaguito

We use a set of TIR images of an explosive ash emission that occurred at Santiaguito volcano (Guatemala) in 2005 (Sahetapy-Engel and Harris, 2009b). The duration of ash emission is about  $\Delta t \simeq 300$  s, and was sampled at 30 Hz.

To analyze the TIR images, we have extracted from the full TIR dataset (Valade et al., 2014) a subset in which the plume can be considered as stationary and fully developed, which starts  $t_{\text{init}} = 45$  s after the beginning of the eruption and ends at  $t_{\text{final}} = 255$  s. The time-averaged image is thus calculated (Fig. 6) and the temperature values are sampled along the axis, at the points represented by the red dots in panel b of Fig. 6. We have then dilated the image to partially correct the error due to the camera inclination. Finally, we have identified a region of about 500 m in width (bounded by the horizontal dashed lines in Fig. 6) where the flow is stationary. The image is then rotated in order to have the plume axis along the  $z$  direction. The resulting image  $T_E(x_i, z_j)$  is shown in Fig 7a). Executing the same operation to the image acquired before the eruption we obtain a matrix within which we have  $I_0(x_i, z_j)$  (Fig 7b).

### 5.3. Two-dimensional inversion procedure

We here present two possible procedures to best-fit the experimental image  $I_E(x, z)$  with the synthetic image  $I_L(x, z)$  produced by the coupled fluid-electromagnetic model. The first method is based on the two-dimensional fit to the thermal image of Figure 7b. Because thermal images are already converted into temperature images, we convert the synthetic intensity image  $I_L$  into a thermal image  $T_L(x_i, z_j)$  by using Eq. (7) with  $\epsilon = 1$  (as in camera settings)

Inversion is achieved by seeking the minimum of a cost function which measures the difference between the synthetic and the experimental images.

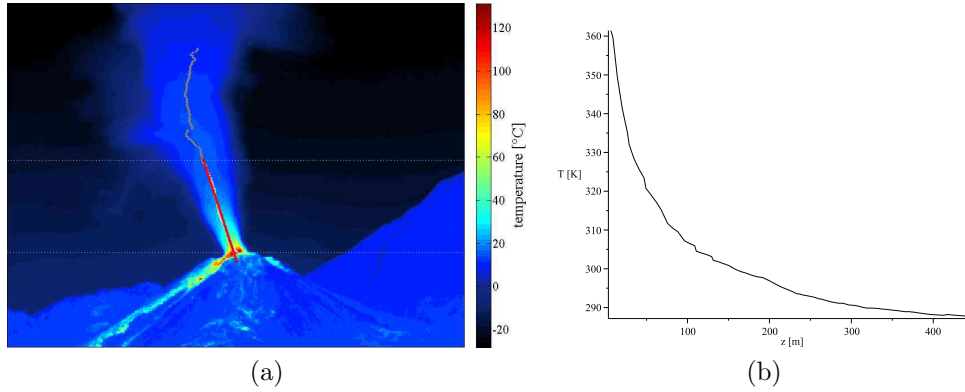


Figure 6: a) Averaged image computed from a set of thermal infrared images recorded with a FLIR camera, imaging the stationary emission of a sustained volcanic ash plume at Santiaguito volcano (Guatemala). The red dots represent the extracted plume axis (Valade et al., 2014). b) Temperature values along the plume axis.

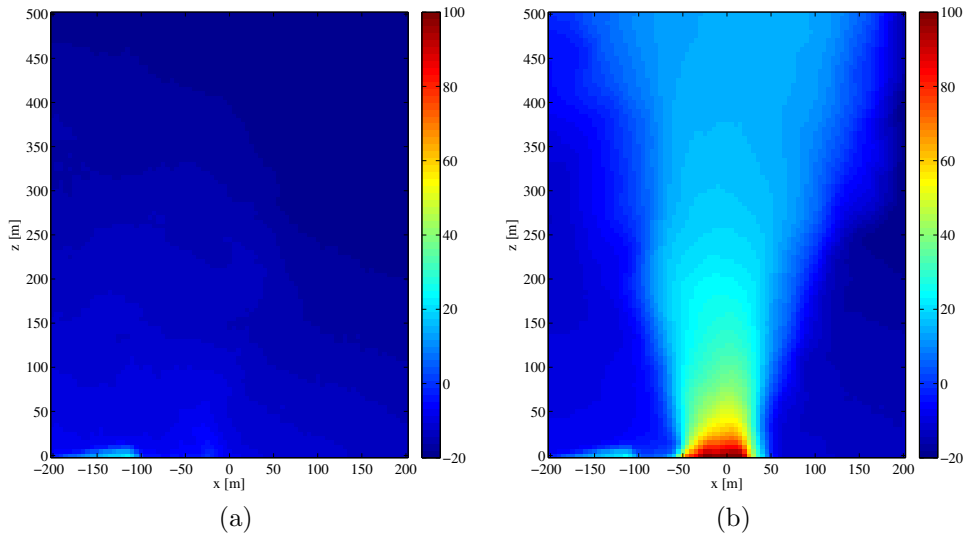


Figure 7: a) Image of the atmosphere above the volcano before the eruption. b) Averaged image of the volcanic eruption. In both images, horizontal and vertical axes represents the position in meters inside the image, the temperature is represented by the color scale in Celsius degrees.



Parameter	Units	Range	Value
$v_q$	–	0.5–0.8	$0.659 \pm 0.004$
$v_m$	–	1.5–3.0	$2.17 \pm 0.04$
$L$	m	25–50	$39.8 \pm 0.2$
$\phi$	–	0.1–0.5	$0.245 \pm 0.002$
$\chi$	–	0.1–1.0	$0.55 \pm 0.02$
$q_m$	–	0.01–0.15	$0.086 \pm 0.003$
$A_m$	m <sup>2</sup> /kg	0.04–0.2	$0.0903 \pm 0.0007$

Table 2: Result of the two-dimensional minimization procedure. Best fit values of the plume parameters. Here we obtained  $\sigma(\mathbf{p}^*) = 6.428^\circ\text{C}$ .

To this end, we have chosen the following residual function:

$$\sigma^2(\mathbf{p}) = \frac{1}{N * M - N_p} \sum_{i=1}^N \sum_{j=1}^M (T_E(x_i, z_j) - T_L(x_i, z_j; \mathbf{p}))^2 \quad (28)$$

where  $\mathbf{p} = (v_q, v_m, L, \phi, \chi, q_m, A_m)$  is the  $N_p$ -dimensional vector of parameters defining  $\sigma^2$  (in this case,  $N_p = 7$ ). The function  $\sigma^2$  must be minimized to obtain the vector of optimal input parameters  $\mathbf{p} = \mathbf{p}^*$  for the plume that best fits the thermal observation. In this application, minimization is performed by deploying a genetic algorithm (implemented in MatLab through the function `ga`), but any minimization procedure can be used. In our case, minimization both inversions have required about 50000 trials which took about 10 s on a laptop. The best fitting plume and the difference (in degrees Celsius) between the synthetic and the observed plume are displayed in Fig. 8. The results of the minimization procedure are also reported in Tab. 2, together with the ranges of variability specified in the search procedure.

In Fig. 9 the projection of  $\sigma(\mathbf{p}^*)$  along each parameter axis, in the neighbours of the minimum, is shown. These plots allow to evaluate the sensitivity of the result on the input parameters and the error associated to the solution. For this test case we obtained  $\sigma = 6.428^\circ\text{C}$ .

#### 5.4. Axial inversion

The second method is based on a one-dimensional fit of the thermal image along the plume axis. The plume axis is defined by a sequence of sampling points in the thermal image (Fig. 6a). By means of image rotation and

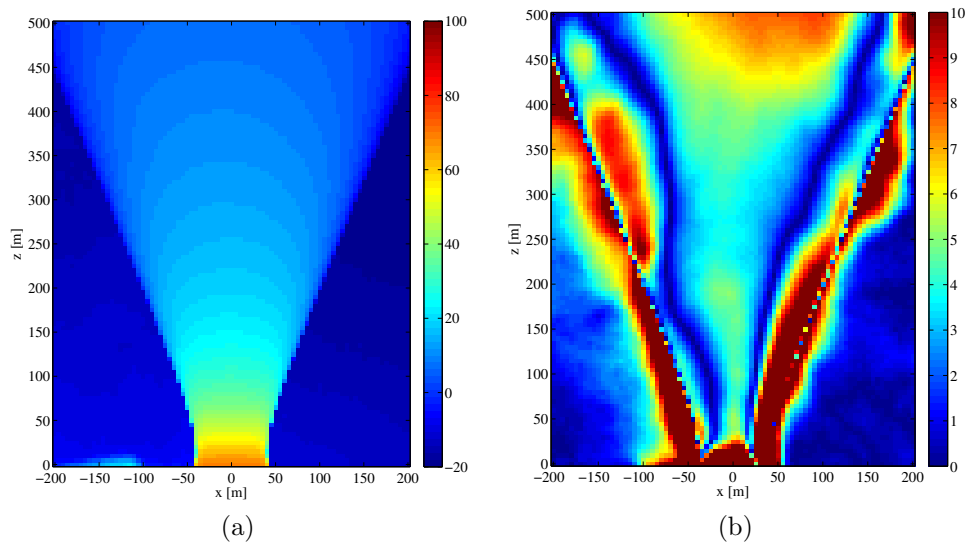


Figure 8: a) Synthetic image of the plume obtained by the two-dimensional fit of Fig. 7b; b) Unsigned difference between the 2D synthetic and the experimental images allowing error quantification and localization. In both images, horizontal and vertical axes represents the position (in meters) inside the image. The color scale represents the temperature in degrees Celsius.

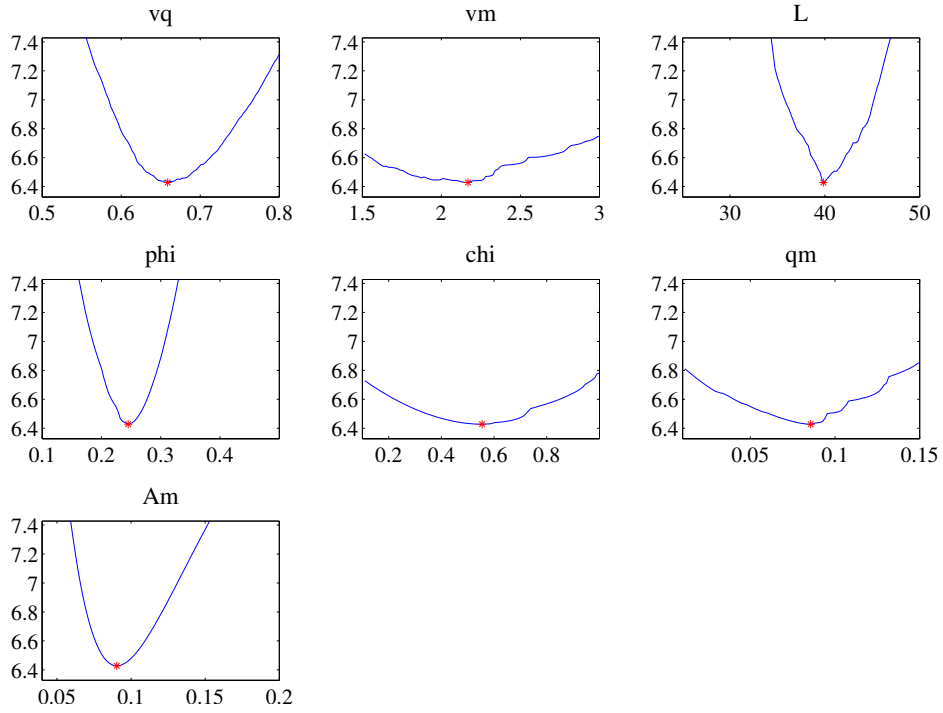


Figure 9: Two-dimensional inversion procedure. Variation of  $\sigma(\mathbf{p})$  of Eq. (28) around  $p^*$  as a function of each single parameter, the others being kept fixed ( $\mathbf{p} = (v_q, v_m, L, \phi, \chi, q_m, A_m)$ ). The red asterisk marks the value of each component of  $\mathbf{p}^*$ ; here we obtained  $\sigma(\mathbf{p}^*) = 6.428^\circ\text{C}$ .

dilation, the value of temperature along a selected region of the plume axis can be expressed as a function of the distance from the vent  $T_E = T_E(z_j)$  (Fig. 6b) .

Using only the axial points has the advantage that the background intensity is no longer important (because the plume is generally opaque along the axis) and we do not have to deal with problem of the plume edge (see the discussion below). However, the entrainment coefficient cannot be extracted using this procedure, so that we need a complementary analysis to evaluate its value. To do this, we can preliminary estimate from the 2D images the plume opening angle ( $\frac{db}{dz}$ ) by defining a threshold in the temperature image (Valade et al., 2014). The entrainment coefficient is thus derived from the plume theory (Ishimine, 2006; Morton et al., 1956) as:

$$k = \frac{5}{6} \frac{db}{dz} .$$

Using this method for this eruption, we obtain  $k = 0.24$ . Alternatively, we can utilize the entrainment coefficient obtained from the two-dimensional fit (Tab. 2)  $k = v_q/2 \simeq 0.329$ .

Subsequently, as for in the two-dimensional case, the synthetic temperature profile  $T_L(z)$  is derived from  $I_\lambda$  by means of Eq.(7). Since  $k$  is independently estimated, the residual function become

$$\sigma^2(\mathbf{p}) = \frac{\sum_{j=1}^N (T_E(z_j) - T_L(z_j; \mathbf{p}))^2}{N - N_p}$$

where now  $\mathbf{p} = (v_m, L, \phi, \chi, q_m, A_m)$  and  $N_p = 6$ . The result of the minimization of this new cost function is displayed in Fig. 10 where the fitting function (solid line) is compared with the experimental thermal data (stars). The results of the minimization procedure are also reported in Tab. 3, together with the ranges of variability specified in the search procedure.

The corresponding 2D image, constructed by applying the top-hat profile to the one-dimensional plume model, and the difference between the optimal synthetic and the experimental images are displayed in Fig. 11.

In Fig. 12 we show the projection of  $\sigma(\mathbf{p}^*)$  along each parameter axis, in the neighbours of the minimum. The error in this case is significantly reduced and all the parameters seem to be better constrained, as also indicated by the much lower value of  $\sigma$ , which, for this test case, is  $\sigma = 0.6596^\circ\text{C}$ .

Finally, the plume input parameters (as obtained by the transformations of Appendix C) are reported in Tab. 4. As a result of the inversion procedure,

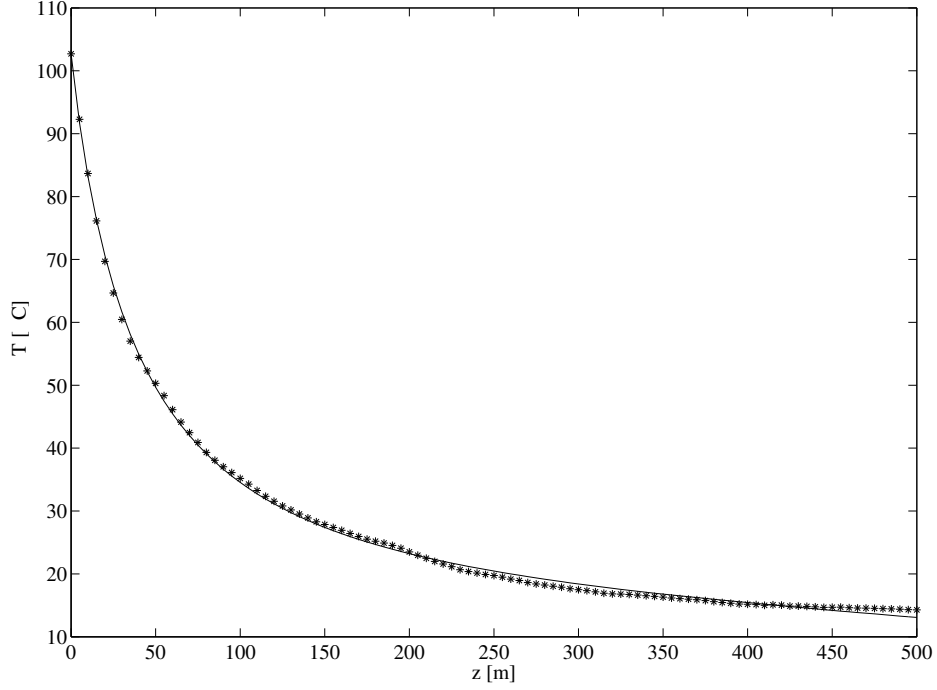


Figure 10: Result of the one-dimensional fit (solid line) of the experimental thermal image along the axis (stars).

Parameter	Units	Range	Value
$v_q$	–	–	$0.659 \pm 0.004$
$v_m$	–	0.1–0.5	$0.34 \pm 0.02$
$L$	m	10–40	$23.8 \pm 0.3$
$\phi$	–	0.1–1.0	$0.579 \pm 0.003$
$\chi$	–	0.5–1.5	$0.73 \pm 0.01$
$q_m$	–	0.1–0.5	$0.29 \pm 0.04$
$A_m$	m <sup>2</sup> /kg	0.1–1.0	$0.215 \pm 0.009$

Table 3: Result of the one-dimensional minimization procedure. Best fit values of the plume parameters. Here we obtained  $\sigma(\mathbf{p}^*) = 0.6596^\circ\text{C}$ .

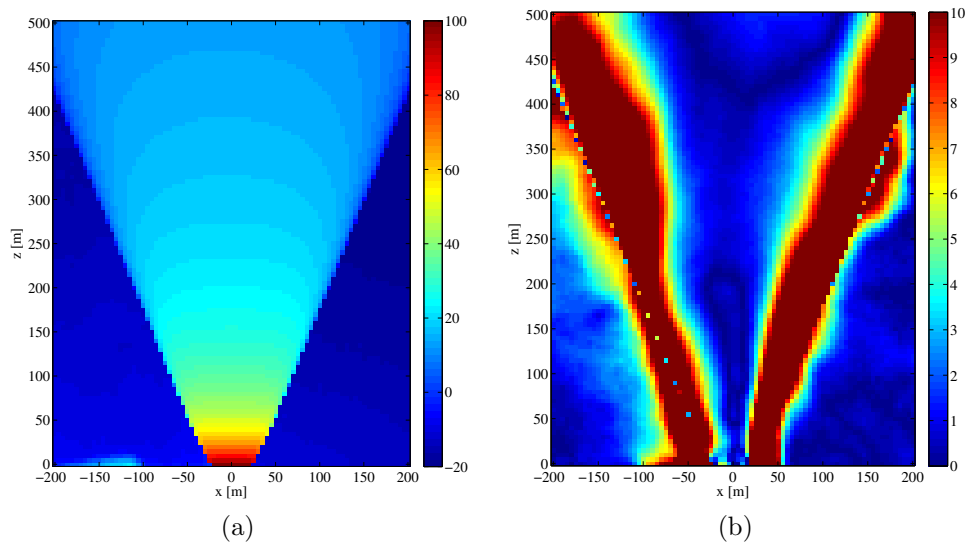


Figure 11: a) Synthetic image of the plume obtained by reconstructing the two-dimensional image from the one-dimensional fit of the axial values in Fig. 7b; b) Unsigned difference between the synthetic and the experimental images allowing error quantification and localization. In both images, horizontal and vertical axes represents the position (in meters) inside the image. The color scale represents the temperature in degrees Celsius.

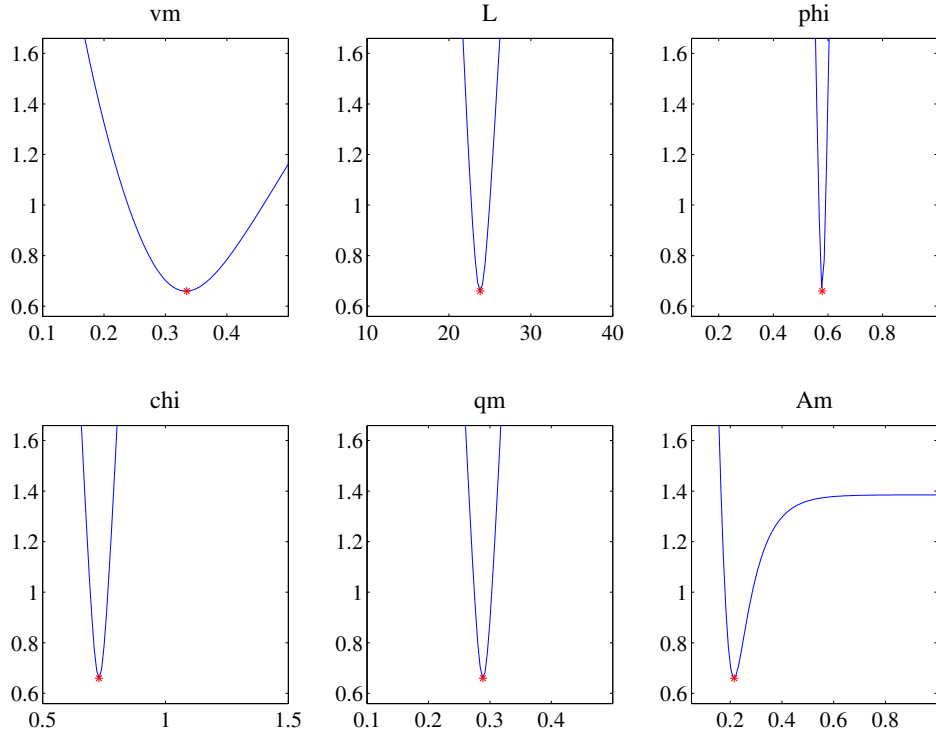


Figure 12: One-dimensional inversion procedure. Variation of  $\sigma(\mathbf{p})$  of Eq. (??) around  $\mathbf{p}^*$  as a function of each single parameter, the others being kept fixed ( $\mathbf{p} = (v_q, v_m, L, \phi, \chi, q_m, A_m)$ ). The red asterisk marks the value of each component of  $\mathbf{p}^*$ ; here we obtained  $\sigma(\mathbf{p}^*) = 0.6596^\circ\text{C}$ .

we are thus able to constrain the eruption mass flow rate (in the stationary regime) as  $\dot{m} = \pi Q = \pi b_0^2 \beta_0 U_0$ . The total erupted mass  $m$  can be obtained by assuming a linear increase of the mass eruption rate between the eruption start and the time  $t_{\text{init}}$  at which the eruption is stationary. Analogously, a linear decrease of the mass eruption rate is assumed between the time  $t_{\text{final}}$  and the end of the eruption. Accordingly,  $m = [\Delta t + (t_{\text{final}} - t_{\text{init}})] \times \pi Q / 2$ . In order to evaluate its error, in Tab. 4 we used an error on  $t$  equal to 10 s.

### 5.5. Parameters error estimate

In order to give a quantitative estimation of the standard error of all the parameters, once we have found  $\mathbf{p}^*$  such that  $\sigma(\mathbf{p}^*)$  is minimum, we assume that the model can be linearized around that  $\mathbf{p}^*$ . In other words, naming  $T_i(\mathbf{p})$  the vector of all the measurements, we suppose that its derivative do not depends on the parameters:  $\partial_{p_k} T_i = Y_{i,k}$ . In such a way, as usually done in the regression analysis (Bates and Watts, 1988), it is possible to formally evaluate all the fit unknowns. In particular, by using Eq. (28) with  $T_L(x_i, y_j) = T_l$  (for  $i = 1, \dots, N$ ;  $j = 1, \dots, M$ ; and  $l = 1, \dots, N * M$ ) we find  $(Y^T Y)_{i,j} = (N * M - N_p) \sigma(\mathbf{p}^*) \partial_{i,j} \sigma$  (for  $i, j = 1, \dots, N_p$ ). It is worth noting that we calculate  $\partial_{i,j} \sigma$  by fitting the surface  $\sigma = \sigma(\mathbf{p})$  with a second order polynomial.

By using the classical formula for the standard error of the parameters,  $\text{se}(\mathbf{p}_i) = \sigma(\mathbf{p}^*) \sqrt{(Y^T Y)_{i,i}^{-1}}$  and by means of error propagation, we are able to find the confidence interval of all the parameters involved in both the axial and two-dimensional fit (reported in Tables 2, 3 and 4).

## 6. Discussion

Comparison of the synthetic images obtained from 2D image fitting (Fig. 8) and 1D fitting (Fig. 11) with the experimental averaged image (Fig. 7), shows that both inversion procedures have their maximum error along the plume boundaries. This is due to the a-priori assumption of a top-hat self-similar profile. This assumption is accurate enough to describe the one-dimensional plume dynamics but is not accurate near the plume margins, where a Gaussian distribution better describes the actual profile. This error is augmented in the coupled model by the fact that 1) the IR absorption depends on the density distribution, so that the top-hat model overestimates the optical thickness near the plume margins and 2) the top-hat model predicts a higher



Parameter	Units	Axial fit	2D fit
$\gamma$	–	$0.862 \pm 0.1$	$0.543 \pm 0.04$
$b_0$	m	$23 \pm 1$	$41.5 \pm 0.3$
$Q_0$	$10^3$ kg/s	$4.1 \pm 0.5$	$6.9 \pm 0.3$
$M_0$	$10^4$ kg m/s <sup>2</sup>	$3.1 \pm 0.7$	$3.1 \pm 0.2$
$U_0$	m/s	$7.5 \pm 0.9$	$4.5 \pm 0.2$
$T_0$	°C	$103 \pm 3$	$69.4 \pm 0.3$
$n_{\text{air}}$	wt. %	$40 \pm 6$	$85 \pm 6$
$n_w$	wt. %	$20 \pm 3$	$4.2 \pm 0.3$
$n_s$	wt. %	$41 \pm 6$	$11.1 \pm 0.7$
$d_s$	mm	$3 \pm 1$	$2.1 \pm 0.6$
$\dot{m}_w$	$10^3$ kg/s	$2.5 \pm 0.7$	$0.9 \pm 0.1$
$\dot{m}_s$	$10^3$ kg/s	$5 \pm 1$	$2.4 \pm 0.3$
$m_w$	$10^5$ kg	$6 \pm 2$	$2.3 \pm 0.4$
$m_s$	$10^5$ kg	$13 \pm 3$	$6 \pm 1$

Table 4: Result of the 1D and 2D minimization procedure: physical input parameters for the coupled model.  $m_e$  and  $m_s$  are the total erupted gas and solid masses.

temperature on the plume margins, with respect to the Gaussian distribution. As a consequence, both effects produce a synthetic image displaying higher temperature at the margins. To minimize this error, the 2D inversion procedure (which considers all pixels) underestimates the axial temperature (and the density) to try to balance the overestimates on the margins. In particular, at  $z = 0$  the error is larger because of the larger temperature contrast at this location. This argument justifies the lower values of temperature and mass flow rate reported in Tab. 4 for the 2D fit with respect to 1D.

The problem associated to the top-hat assumption is reduced when we fit only the axial values, because the integral of the absorption coefficient (i.e. the optical thickness) takes into account the whole density and temperature distribution across the plume. Therefore, the error is significantly lower in a wide region around the axis, whereas larger errors are concentrated near the margins. The better accuracy of the 1D fitting procedure is confirmed by the observation that the error  $\sigma$  is comparable to the instrumental accuracy, which is about  $0.5^\circ\text{C}$ . In the 2D case, the value of  $\sigma$  corroborates the conclusion that the model is not fully suited to represent the 2D shape of the plume image.

The top-hat assumption is thus more satisfactory when axial inversion is performed; a more accurate description of the plume profile is required to invert the fully 2D image. While assuming a Gaussian profile would be conceptually equivalent to the adopted top-hat hypothesis, the inversion would be computationally more intense, because the coupled model cannot be written analytically. The above observations also allow us to assert that the electromagnetic model is accurate enough to represent the IR emission/absorption balance throughout the plume and the error is mainly associated to application of the oversimplified fluid-dynamic model.

Despite these differences, the results of the two procedures are coherent and indicate a mass eruption rate of  $7.75 \times 10^3$  in 1D and  $3.31 \times 10^3$  in 2D. The observed ash plume has a gas content at  $z = 0$  of 59 wt.% in 1D and 89 wt.% in 2D. It is worth recalling here that  $z = 0$  does not correspond to the actual vent level but instead to the minimum quota of the analyzed thermal image. At  $z = 0$  the amount of entrained air is already significant (40 wt. % in 1D and 85 wt.% in 2D), and it is probably associated to the specific behavior of the ash eruptions at Santiaguito which occur through a circular annulus surrounding the conduit plug (Bluth and Rose, 2004; Sahetapy-Engel and Harris, 2009b). This can be responsible for the efficient entrainment of atmospheric air, a modification of the gas thrust region and the rapid lowering

of the mixture temperature (about 100°C in 1D and 70°C in 2D). The mass fraction of erupted gas (here assumed to be only water vapor), with respect to the total erupted mass, is in any case fairly high (32 wt. % in 1D and 27 wt. % in 2D). The low ash-to-air mass ratio recovered from the inversion model are likely to be the result of emission through a porous system of cracks forming a circular vent structure (Bluth and Rose, 2004; Sahetapy-Engel and Harris, 2009a), so that air becomes entrapped within the “empty” center of the emission, thereby increasing the amount of air ingestion over cases where it enters only across the plume outer surface. The resulting ash-to-air mass ratio is low, so that the plume is dominated by heated air, with a very minor dense ash component, enhancing the buoyancy and explaining why an explosion of such low violence (mean at-vent velocities being just 25 m s<sup>-1</sup>) can ascend to heights of between 2 and 4 km above the vent.

Finally, the estimated Sauter diameter is also comparable in the two procedures. To compare the reported values with field observations, by assuming a lognormal particle distribution with  $\sigma_{\text{gsd}} = 1.225$  (based on the range 275 – 950  $\mu\text{m}$  found by Wilson and Self (1980) from insitu plume sampling on filters from aircraft) and by using Eq. (6) we find the mean particle diameter  $\bar{d} = 768 \mu\text{m}$  (in 1D) and  $\bar{d} = 507 \mu\text{m}$  (in 2D).

### 6.1. Plume color and visibility

It is worth noting that in Fig. C.13 there are some wavelength in the visible spectral window ( $\lambda < 780 \mu\text{m}$ ) where the absorption coefficient of atmospheric water vapor at standard density reaches 1 m<sup>-1</sup>, comparable with  $A_w$  in the IR wavelength window considered in this paper. Moreover, the specific absorption of the ash particles is also of the same order of magnitude,  $A_s \simeq 1 \text{ m}^2/\text{kg}$ , because the assumption  $d \gg \lambda$  we used to evaluate it is even more satisfied in the visible waveband. Therefore, we can roughly say that 1) a high-temperature water-ash plume can be “viewed” by a thermal camera in the 8-14  $\mu\text{m}$  waveband if we can see it with our eyes 2) a high-temperature water-ash plume that is opaque to our eyes is also opaque to the thermal camera 3) the plume optical thickness will be dominated by the water if  $n_w \gg n_s$  or by the particles if  $n_w \ll n_s$ . As suggested by intuition, in the former case we will see a “white” plume, in the latter a black plume. Obviously, in intermediate conditions we will see a lighter or darker gray. Now, looking at eruptions occurred at Santiaguito, the plume often appear quite light. This observation supports the argument that the erupted mixture has a quite high concentration of water.

## 7. Conclusion

We have developed an inversion procedure to derive the main plume dynamic parameters from a sequence of thermal infrared (TIR) images. The procedure is based on the minimization of the difference between the time-averaged experimental image and a synthetic image built upon a fluid-dynamic plume model coupled to an electromagnetic emission/absorption model. The method is general and, in principle, can be applied to the spatial distribution of particle concentration and temperature obtained by any fluid-dynamic model, either integral or multidimensional, stationary or time-dependent, single or multiphase.

The fluid-dynamic model adopted in this work assumes self-similarity of the plume horizontal profile and kinetic and thermal equilibrium between the gas and the particulate phases. It is solved analytically in the approximation of negligible influence of atmospheric stratification (which holds below the maximum plume height considered here) and small density contrast (valid far enough above the vent) to obtain the flow parameters as a function of the height  $z$  above the vent. The electromagnetic model computes the radiated intensity from a given spatial distribution of particle concentration and temperature, assuming that particles are coarser than the radiation wavelength (about  $10\ \mu\text{m}$ ) and neglecting scattering effects. In the approximation of a homogeneous plume (top-hat profile) and negligible atmospheric absorption, the coupling of the two models can be achieved analytically and allows construction of a synthetic TIR image of a volcanic plume starting from a set of vent conditions, namely the vent radius  $b_0$ , velocity  $U_0$ , temperature  $T_0$ , gas mass ratio  $n_0$ , entrainment coefficient  $k$  and the equivalent Sauter diameter  $d_s$  of the particle size distribution. The latter is equivalent to the average particle diameter of a monodisperse distribution having the same surface area (across a section) of the polydisperse cloud. The minimization method, in the case analyzed here, can be applied to the single image obtained by time-averaging the sequence of TIR observations and the inversion can be performed in a few seconds on a laptop by exploiting any standard non-linear fitting software.

A test application to an ash eruption at Santiaguito demonstrates that the inversion based on the one-dimensional axial fit is preferable, because the error entailed in the inversion procedure is lower. This is due to the top-hat assumption which overestimates density and temperature at the plume margins. The key eruption parameters of the observed eruption are obtained,

namely the mass flow rate of the gas and particulate phases, the mixture temperature and the mean Sauter diameter of the grain size distribution.

The method developed here to recover ash plume properties is fast and robust. This suggests its potential applications for real-time estimation of ash mass flux and particle size distribution, which is crucial for model-based projections and simulations. By streaming infrared data to a webtool running, in real-time, the model could provide the input parameters required for ash dispersion models run by VAACs.

The algorithm could also be easily applied to more complex geometric configuration (e.g., to a bent plume in a wind field – Woodhouse et al. (2013)) and atmospheric conditions (e.g., in presence of a significant amount of water vapour), or to more realistic plume models (e.g., assuming a Gaussian plume profile). In such cases, the coupled model should be solved numerically. It is worth noting that the calibration of the background atmospheric infrared intensity and the information on the atmospheric absorption can be critical in the applications and we recommend experimentalists to consider their effects during the acquisition campaigns. Also, the intensity image would be preferable with respect to the temperature image, which is derived from automatic onboard processing by commercial thermal cameras. Finally, it is worth noting that a rigorous validation of the direct model (i.e., the generation of the synthetic image) must still be achieved. Unfortunately, we could not find detailed experimental measurements of the TIR radiation from a turbulent gas-particle plume under controlled injection conditions. This would be extremely useful to calibrate the coupled forward model and to better understand plume visibility issues.

## **Acknowledgements**

This work presents results achieved in the PhD work of the first author (M.C.), carried out at Scuola Normale Superiore and Istituto Nazionale di Geofisica e Vulcanologia. Support by the by the European Science Foundation (ESF), in the framework of the Research Networking Programme MeM-oVolc, is also gratefully acknowledged. AH (and SV until June 2013) was supported by le Région Auvergne and FEDER.

Gas species	$R$	$C_P$
Water vapor	462	1862
Atmospheric air	287	998
Ash	–	1100

Table A.5: Thermo-physical parameters of the plume components.

### Appendix A. Thermodynamics of the dusty gas

Closure of Eq. 13 requires the specification of the thermodynamics of all components of the eruptive mixture. We indicate with  $C$  the specific heats at constant pressure, that we assume constant (see Tab. A.5). The dusty-gas specific heat is expressed as a function of its components as:

$$C_\beta = \frac{1}{\beta}(\rho_s C_s + \rho_e C_e + \rho_\alpha C_\alpha) \quad (\text{A.1})$$

which, in terms of the conserved variables, can be written as:

$$C_\beta = C_\alpha + \frac{Q_s}{Q}(C_s - C_\alpha) + \frac{Q_e}{Q}(C_e - C_\alpha). \quad (\text{A.2})$$

We indicate with  $R$  the gas constants (see Tab. A.5). The dusty-gas constant is expressed as a function of its components as:

$$R_g = R_\alpha + \frac{\rho_e}{\beta - \rho_s}(R_e - R_\alpha) = R_\alpha + \frac{Q_e}{Q - Q_s}(R_e - R_\alpha). \quad (\text{A.3})$$

The following quantities are also defined:  $\chi_s = C_s/C_\alpha$ ,  $\chi_e = C_e/C_\alpha$ ,  $\psi_e = R_e/R_\alpha$ .

Finally, following Woods (1988), the density  $\beta$  of the dusty gas is expressed as a function of the conserved variables as:

$$\frac{1}{\beta} = \frac{1 - n}{\sigma} + \frac{nR_g T_\beta}{p} = \frac{1}{\hat{\rho}_s} \frac{Q_s}{Q} + \left(1 - \frac{Q_s}{Q}\right) \frac{R_g T_\beta}{p}, \quad (\text{A.4})$$

where the particle (average) material density is taken as constant  $\hat{\rho}_s = 1600\text{kg/m}^3$ .

## Appendix B. Variable transformation

The dimensioned variables can be expressed in terms of the non-dimensional variables  $(q, m, f)$  by the following transformations:

$$\beta = \alpha \frac{q(q + \chi q_m)}{(\phi + q)(q - q_m)} \quad (\text{B.1})$$

$$b = L \sqrt{\frac{\alpha_0}{\alpha} \frac{q(\phi + q)(q - q_m)}{m(q + \chi q_m)}} \quad (\text{B.2})$$

$$U = U_0 \frac{m}{q} \quad (\text{B.3})$$

$$T_\beta = T_\alpha \frac{\phi + q}{q + \chi q_m} \quad (\text{B.4})$$

## Appendix C. Parameter inversions

The solution of the plume model Eq. 22 in non-dimensional form is function of the boundary values and model parameters,  $(v_q, v_m, q_m, \phi, \chi, L)$ . The inversion procedure described in Sect. 5 provides the set of parameters which minimizes the difference between the synthetic and the experimental image. We here report the transformation needed to obtain the equivalent set of eruption parameters.

We first use Eq. (20) together with the expression for  $L = Q_0/\sqrt{\alpha_0 M_0}$  to obtain:

$$M_0 = \frac{g\phi\alpha_0}{v_m}(1 - \gamma) \quad (\text{C.1})$$

$$Q_0 = \sqrt{\alpha_0 M_0} L \quad (\text{C.2})$$

$$U_0 = \frac{M_0}{Q_0} \quad (\text{C.3})$$

By means of Eqs. (B.2) and (B.4), putting  $(q = 1, m = 1)$  and  $\alpha = \alpha_0$  at  $z = 0$ , we also obtain:

$$b_0 = \sqrt{\frac{(1 + \phi)(1 - q_m)}{1 + \chi q_m}} L \quad (\text{C.4})$$

$$T_0 = T_{\alpha_0} \frac{\phi + 1}{1 + \chi q_m} \quad (\text{C.5})$$

Finally, the composition of the eruptive mixture can be reconstructed by noting that:

$$q_m = n_s - (\psi_w - 1)n_w \quad (\text{C.6})$$

$$\chi = \frac{(\chi_s - 1)n_s - (\chi_w - 1)n_w}{q_m} \quad (\text{C.7})$$

where we have assumed that the erupted gas is composed of water vapour (subscript  $w$ ). The system can be solved to obtain the mass fractions of ash, volcanic gas and atmospheric gas at  $z = 0$ :

$$n_w = \frac{(1 + \chi - \chi_s)q_m}{(\chi_s - 1)(\psi_w - 1) + (\chi_w - 1)} \quad (\text{C.8})$$

$$n_s = q_m \frac{\chi(\psi_w - 1) + (\chi_w - 1)}{(\chi_s - 1)(\psi_w - 1) + (\chi_w - 1)} \quad (\text{C.9})$$

$$n_\alpha = 1 - n_w - n_s. \quad (\text{C.10})$$

Note that, in general, the gas mass fraction in the mixture at  $z = 0$  is  $n_0 = n_w + n_\alpha$ . Since the quota  $z = 0$  may not correspond to the vent quota (it is better defined as the quota where the plume starts to be self-similar and stationary),  $n_0$  in general does not correspond to the gas content in the eruptive mixture but may also contain the fraction  $n_\alpha$  of entrained air.

Finally, the equivalent Sauter diameter of the grain size distribution can be derived by the absorption coefficient  $A_m$  by assuming that the absorption by atmospheric air is negligible. In such case, in Eq. (23) the specific absorption coefficient can be written as:

$$A_m = A_s q_s + A_w q_w = A_s n_s + A_w n_w.$$

Therefore, knowing the specific absorption coefficient of water vapour  $A_w$  and the components mass fraction, the specific absorption coefficient for particles  $A_s$  can be derived from this expression. By noting that  $A_s = \frac{3}{2d_s \hat{\rho}_s}$ , this can be used to estimate  $d_s$ . Please notice that the absorption coefficient for water should be estimated by the experimentalists as the convolution of the detector response function with the spectral absorption coefficient for the pure gas. For example, in the case of atmospheric water vapour, in order to evaluate  $A_w$ , we have to execute the convolution of the spectral response of our camera (cf. Fig. C.13a for an example) and the absorption spectrum of



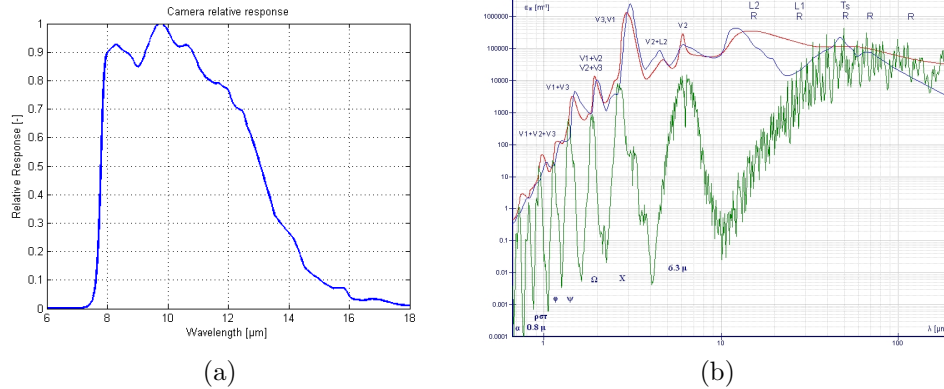


Figure C.13: a) An example of a typical spectral response of a FLIR camera in the spectral window  $7 \div 14 \mu\text{m}$ . b) *From Wikipedia*: Absorption spectrum (attenuation coefficient vs. wavelength) of liquid water (red), atmospheric water vapor (green) and ice (blue line) between 667 nm and  $200 \mu\text{m}$ . The plot for vapor is a transformation of data *Synthetic spectrum for gas mixture 'Pure H<sub>2</sub>O'* (296K, 1 atm) retrieved from Hitran on the Web Information System.

the atmospheric water vapour (Fig. C.13b). Throughout the paper we used the value  $A_w = 1\text{m}^2/\text{kg}$  that, as we can see in Fig. C.13, is the right order of magnitude for the absorption coefficient of atmospheric water vapour.

## References

- Bates, D.M., Watts, D.G., 1988. Nonlinear regression: iterative estimation and linear approximations. Wiley Online Library.
- Bluth, J.G.S., Rose, W.I., 2004. Observations of eruptive activity at santiaquito volcano, guatemala. J. Volcanol. Geoth. Res. 136, 297–302.
- Bombrun, M., Barra, V., Harris, A., 2013. Particle detection and velocity prediction for volcanic eruptions: a preliminary study, IAVCEI General Assembly, Kagoshima, Japan.
- Bonadonna, C., Folch, A., Loughlin, S., Puempel, H., 2012. Future developments in modelling and monitoring of volcanic ash clouds: outcomes from

- the first iavcei-wmo workshop on ash dispersal forecast and civil aviation. *Bull. Volcanol.* 74, 1–10.
- Carrier, G., 1958. Shock waves in a dusty gas. *J. Fluid Mech.* 4, 376–382.
- Cerminara, M., 2014. Multiphase flows in volcanology. PhD thesis. To appear.
- Clarke, a.B., Voight, B., Neri, a., Macedonio, G., 2002. Transient dynamics of vulcanian explosions and column collapse. *Nature* 415, 897–901. doi:10.1038/415897a.
- Deligne, N., Coles, S., Sparks, R., 2010. Recurrence rates of large explosive volcanic eruptions. *J. Geophys. Res.* 115, B06203.
- Delle Donne, D., Ripepe, M., 2012. High-frame rate thermal imagery of strombolian explosions: Implications for explosive and infrasonic source dynamics. *J. Geophys. Res.* 117. doi:10.1029/2011JB008987.
- Druitt, T.H., Kokelaar, B.P., 2002. The eruption of soufrière hills volcano, montserrat, from 1995 to 1999, Geological Society of London.
- Fanneløp, T., Webber, D., 2003. On buoyant plumes rising from area sources in a calm environment. *J. Fluid Mech.* 497, 319–334.
- Giberti, G., Jaupart, C., Sartoris, G., 1992. Steady-state operation of stromboli volcano, italy: constraints on the feeding system. *Bull. Volcanol.* 54, 535–541.
- Hänel, G., Dlugi, R., 1977. Approximation for the absorption coefficient of airborne atmospheric aerosol particles in terms of measurable bulk properties. *Tellus* 29, 75–82.
- Harris, A., 2013. Thermal Remote Sensing of Active Volcanoes.
- Harris, A., Ripepe, M., 2007. Temperature and dynamics of degassing at stromboli. *J. Geophys. Res.* 112, B03205.
- Harris, A., Ripepe, M., Hughes, E., 2012. Detailed analysis of particle launch velocities, size distributions and gas densities during normal explosions at stromboli. *J. Volcanol. Geoth. Res.* .

- Ishimine, Y., 2006. Sensitivity of the dynamics of volcanic eruption columns to their shape. *Bull. Volcanol.* 68, 516–537.
- Johnson, J.B., Harris, A.J., Sahetapy-Engel, S.T., Wolf, R., Rose, W.I., 2004. Explosion dynamics of pyroclastic eruptions at santiaguito volcano. *Geophys. Res. Lett* 31, L06610.
- Kaminski, E., Tait, S., Carazzo, G., 2005. Turbulent entrainment in jets with arbitrary buoyancy. *J. Fluid Mech.* 526, 361–376.
- List, E.J., 1982. Turbulent jets and plumes. *Annu. Rev. Fluid Mech.* 14, 189–212.
- Marble, F.E., 1970. Dynamics of dusty gases. *Ann. Rev. Fluid Mech.* 2, 397–446.
- Mastin, L., Guffanti, M., Servranckx, R., Webley, P., Barsotti, S., Dean, K., Durant, A., Ewert, J., Neri, A., Rose, W., et al., 2009. A multidisciplinary effort to assign realistic source parameters to models of volcanic ash-cloud transport and dispersion during eruptions. *J. Volcanol. Geoth. Res.* 186, 10–21.
- Mie, G., 1908. Pioneering mathematical description of scattering by spheres. *Ann. Phys* 25, 337.
- Modest, M., 2003. Radiative heat transfer. Academic press.
- Morton, B.R., 1959. Forced plumes. *J. Fluid Mech.* 5, 151–163. doi:10.1017/S002211205900012X.
- Morton, B.R., Taylor, G., Turner, J.S., 1956. Turbulent gravitational convection from maintained and instantaneous sources. *Proc. R. Soc. Lon. A* 234, 1–23.
- Newhall, C.G., Self, S., 1982. The volcanic explosivity index (vei) an estimate of explosive magnitude for historical volcanism. *J. Geophys. Res.* 87, 1231–1238. URL: <http://dx.doi.org/10.1029/JC087iC02p01231>, doi:10.1029/JC087iC02p01231.
- Papanicolaou, P.N., List, E.J., 1988. Investigations of round vertical turbulent buoyant jets. *J. Fluid Mech.* 195, 341–391.

- Patrick, M., Harris, A., Ripepe, M., Dehn, J., Rothery, D., Calvari, S., 2007. Strombolian explosive styles and source conditions: insights from thermal (flir) video. *Bull. Volcanol.* 69, 769–784.
- Plourde, F., Pham, M.V., Kim, S.D., Balachandar, S., 2008. Direct numerical simulations of a rapidly expanding thermal plume: structure and entrainment interaction. *J. Fluid Mech.* 604, 99–123.
- Ramsey, M., Harris, A., 2012. Volcanology 2020: How will thermal remote sensing of volcanic surface activity evolve over the next decade? *J. Volcanol. Geoth. Res.* .
- Ricou, F., Spalding, D., 1961. Measurements of entrainment by axisymmetrical turbulent jets. *J. Fluid Mech.* 11, 21–32.
- Sahetapy-Engel, S.T., Harris, A.J., 2009a. Thermal structure and heat loss at the summit crater of an active lava dome. *Bull. Volcanol.* 71, 15–28.
- Sahetapy-Engel, S.T., Harris, A.J.L., 2009b. Thermal-image-derived dynamics of vertical ash plumes at santiaguito volcano, guatemala. *Bull. Volcanol.* 71, 827–830.
- Sawyer, G.M., Burton, M.R., 2006. Effects of a volcanic plume on thermal imaging data. *Geophys. Res. Lett.* 33.
- Scollo, S., Boselli, A., Coltelli, M., Leto, G., Pisani, G., Spinelli, N., Wang, X., 2012. Monitoring etna volcanic plumes using a scanning lidar. *Bulletin of volcanology* 74, 2383–2395.
- Spampinato, L., Calvari, S., Oppenheimer, C., Boschi, E., 2011. Volcano surveillance using infrared cameras. *Earth-Science Reviews* 106, 63–91.
- Sparks, R., Bursik, M., Carey, S., Gilbert, J., Glaze, L., Sigurdsson, H., Woods, A., 1997. *Volcanic plumes*. Wiley.
- Stohl, A., Prata, F., Elbern, H., Scollo, S., Varghese, S., 2010. Description of some european ash transport models, in: Zehner, C. (Ed.), *Monitoring Volcanic Ash from Space. Proceedings of the ESA-EUMETSAT workshop on the 14 April to 23 May 2010 eruption at the Eyjafjoll volcano, South Iceland*.

- Tupper, A., Kinoshita, K., Kanagaki, C., Iino, N., Kamada, Y., 2003. Observations of volcanic cloud heights and ash-atmosphere interactions, in: WMO/ICAO Third International Workshop on Volcanic Ash, Toulouse, France, September.
- Valade, S.A., Harris, A.J.L., Cerminara, M., 2014. Plume ascent tracker: Interactive matlab software for analysis of ascending plumes in image data. *Computers & Geosciences* .
- Wilson, L., 1976. Explosive volcanic eruptions—III. Plinian eruption columns. *Geophys. J. Roy. Astr. S.* 45, 543–556.
- Wilson, L., Self, S., 1980. Volcanic explosion clouds: Density, temperature, and particle content estimates from cloud motion. *Journal of Geophysical Research: Solid Earth (1978–2012)* 85, 2567–2572.
- Woodhouse, M., Hogg, A., Phillips, J., Sparks, R., 2013. Interaction between volcanic plumes and wind during the 2010 eyjafjallajökull eruption, iceland. *J. Geophys. Res.* 118, 92–109.
- Woods, A., 1988. The fluid dynamics and thermodynamics of eruption columns. *Bull, Volcanol.* 50, 169–193.
- Woods, A., Bursik, M., 1991. Particle fallout, thermal disequilibrium and volcanic plumes , 559–570.